

Bayesian Parameter Inference and Uncertainty Quantification for a Computational Pulmonary Hemodynamics Model Using Gaussian Processes

Amirreza Kachabi¹, Sofia Altieri Correa¹, Naomi C. Chesler¹, Mitchel J. Colebank^{1,2*}

1) Edwards Lifesciences Foundation Cardiovascular Innovation and Research Center, Department of Biomedical Engineering, University of California, Irvine, Irvine, CA, USA

2) Department of Mathematics, University of South Carolina, Columbia, SC, USA

ORCIDs of authors:

Amirreza Kachabi: 0009-0005-2627-942X

Naomi C. Chesler: 0000-0002-7612-5796

Mitchel J. Colebank: 0000-0002-2294-9124

* Corresponding author

Email: mjcolebank@sc.edu (MJC)

Abstract

Patient-specific modeling is a valuable tool in cardiovascular disease research, offering insights beyond what current clinical equipment can measure. Given the limitations of available clinical data, models that incorporate uncertainty can provide clinicians with better guidance for tailored treatments. However, such modeling must align with clinical time frameworks to ensure practical applicability. In this study, we employ a one-dimensional fluid dynamics model integrated with data from a canine model of chronic thromboembolic pulmonary hypertension (CTEPH) to investigate microvascular disease, which is believed to involve complex mechanisms. To enhance computational efficiency during model calibration, we implement a Gaussian process emulator. This approach enables us to explore the relationship between disease severity and microvascular parameters, offering new insights into the progression and treatment of CTEPH in a timeframe that is compatible with a reasonable clinical timeframe.

Keywords

Statistical emulation, Uncertainty quantification, One-dimensional fluid mechanics, hemodynamics, CTEPH

1 Introduction

Computational simulations have emerged as valuable tools in the medical field, offering critical insights that are impractical or infeasible to obtain through clinical measurements. These advanced models can be tailored to individual patients and may lead to personalized treatments based on their predictions. However, before making decisions based on these model predictions, the models must be calibrated using patient-specific data. Model calibration, also referred to as an inverse problem or parameter estimation, involves assessing the consistency between patient-derived measurements and the predictions generated by the model. Formal inference requires an assumption about the statistical nature of the parameters. Different studies in the biosciences have attempted to calibrate their models using either a frequentist, classical statistics approach (Kachabi et al., 2023; Taylor-Lapole et al., 2024; Zambrano et al., 2018) or a Bayesian approach (Huang et al., 2006; Păun et al., 2018; Wentworth et al., 2018). While both methods can provide direct mechanisms for uncertainty quantification (UQ) in the model predictions, Bayesian methods offer deeper, intuitive insights for clinicians and scientists. These models often involve numerically solving partial differential equations (PDEs) to calculate the posterior density for UQ, which can be computationally intensive, sometimes taking several months (Hu et al., 2024; Massoud, 2019). This makes it challenging to implement within a reasonable clinical timeframe, which would be on the order of minutes or a few hours.

One way to accelerate PDE solutions and solve the inverse problem is using statistical emulation (Conti & O'Hagan, 2010; Mora et al., 2024). Emulation, which approximates the expensive simulator with a computationally cheaper model, offers an efficient approach to approximating complex systems, significantly lowering the cost and time of simulations and enables the solution of large-scale or high-dimensional problems. Statical emulations are particularly useful for real-time applications and provide valuable insights into system behavior while ensuring accurate approximation of inverse solutions. Several studies used different techniques to build emulators, such as neural networks (NNs) (Beliaev & Smirnov, 2023), Gaussian processes (GPs) (Di Achille et al., 2018) and polynomial chaos expansions (PCEs) (Marzouk & Najm, 2009). While PCEs are better suited for low-dimensional problems (Lu et al., 2015), GPs excel in high-dimensional spaces and perform well with small training datasets, whereas NNs require large datasets for training (Ghafariasl et al., 2024; Zanjani Foumani et al., 2023).

Complex hemodynamic models are particularly useful in understanding biomechanically complex diseases, such as pulmonary hypertension (PH). This condition is characterized by an elevated mean blood pressure (exceeding 20 mmHg) in the main pulmonary artery (MPA) at rest. It is commonly associated with vascular remodeling of both large and small pulmonary arteries. Among the various subgroups of PH, chronic thromboembolic pulmonary hypertension (CTEPH) is a notable form that occurs when blood clots (thromboembolisms) obstruct the pulmonary arteries, leading to increased pulmonary blood pressure. While most cases of CTEPH can be effectively treated with surgery, persistent PH can occur in patients suffering from additional

microvascular disease (Galiè & Kim, 2006). The severity of small-vessel arteriopathy has been proposed to have a significant impact on the persistence of PH and survival following surgery (Gerges et al., 2020). However, the current standard preoperative assessment of CTEPH cannot detect the presence of small-vessel disease reliably, nor does it accurately predict the postoperative outcome. Therefore, there is an unmet need for assessing the degree and presence of small-vessel disease in CTEPH, inviting new computational approaches to elucidating this mechanism.

Thus, the goal of this study is to use computational hemodynamic modeling to investigate microvascular disease in CTEPH and examine the impacts of CTEPH on the microvasculature model parameters. To achieve this goal, we first build an emulator using GPs for a one-dimensional (1D) fluid dynamics model of the pulmonary circulation using previously published canine data. For each subject, we construct asymmetric, binary-structured trees at the end of the terminal large vessels to model the microvasculature. Then, using GP emulators, we calibrate the model to measured data in a Bayesian framework. We determine potential correlations between these parameters and the severity of the disease. Lastly, we account for the uncertainties in the simulated outputs by propagating uncertainties via the parameter posterior distributions. We provide an effective framework for combining limited, noisy data with a complex hemodynamic model, and extract uncertainty-aware parameter estimates and output uncertainty.

2 Methods

2.1 Data collection

We use animal data originally collected and reported in Mulchrone et al. (2019). In brief, five male canines were subjected to repeated microsphere injections into the pulmonary circulation to imitate CTEPH development. Additional details can be found in Mulchrone et al. (2019). The data used from the animal study include magnetic resonance angiography (MRA) data, systolic and diastolic main pulmonary artery (MPA) pressure ($p_{sys}^{MPA}, p_{dia}^{MPA}$), time series flow in the MPA, left pulmonary (LPA), and right pulmonary (RPA) arteries ($\mathbf{q}^{MPA}, \mathbf{q}^{LPA}, \mathbf{q}^{RPA}$), and time series MPA area (\mathbf{A}^{MPA}) in both pre-CTEPH (baseline) and post-CTEPH (CTEPH) stages. We use the baseline MRA data to reconstruct a computational domain for each animal, similar to our previous study (Kachabi et al., 2023). The computational domain includes a connected network of large arteries, which are described by a connectivity matrix and vessel dimensions (i.e., length and radius). We note that, in contrast to this prior study, we use the baseline geometry for all simulations, thus isolating the differences between baseline and CTEPH results (e.g., differences in material properties) from changes in large vessel dimensions or connectivity obtained on sequential MR imaging. The microcirculation, which is infeasible to identify by MR imaging, is described using the structured tree model, described later (Olufsen, 1999).

2.2 Data processing

We ensured that the average measured flow was conserved by shifting the measured MPA flow to match the averaged RPA and LPA flows. We also adjusted the minimum flow in certain animals to ensure that the input flow started close to zero for all cases, as there were no reported cases of pulmonary valve regurgitation. Subjects 2 (S2) and S4 had clear measurement errors; we rebuilt these waveforms while keeping the maximum and minimum MPA area values the same. Lastly, for S3 at baseline, there was an abnormally long recorded cardiac cycle of 1.4 seconds, where values from 0.8 to 1.4 seconds were constant zero flow. Therefore, we truncated the cardiac cycle to 0.8 seconds, consistent with the cardiac cycles of other animals.

2.3 Governing equations and boundary conditions

We simulated pressure, flow, and vessel area in the vasculature captured by MR by solving the 1D Navier-Stokes equations. We assume that all blood vessels are straight, cylindrical, and impermeable, and that blood flow through the arterial network is axisymmetric, incompressible, Newtonian, and laminar. We then have the governing equations

$$\frac{\partial Q}{\partial x} + \frac{\partial A}{\partial t} = 0, \quad (1)$$

$$\frac{\partial Q}{\partial t} + \frac{(\gamma + 2)}{(\gamma + 1)} \frac{\partial}{\partial x} \left(\frac{Q^2}{A} \right) + \frac{A}{\rho} \frac{\partial P}{\partial x} = - \frac{2\pi\mu(\gamma + 2) Q}{\rho A}, \quad (2)$$

where x (cm) and t (s) represent the axial and temporal coordinates, and $P(x, t)$ is the transmural blood pressure (g/cm s^2) (Olufsen et al., 2000). $Q(x, t)$ is the volumetric flow (mL/s) and $A(x, t)$ is the cross-sectional area (cm^2). The parameters ρ and μ are blood density and dynamic viscosity that are set 1.03 (g/mL) and 0.03 (g/cm s), respectively (Kamiya & Togawa, 1980). Furthermore, we assumed the shape of the blood flow velocity follows a power-law axial profile. We assume $\gamma = 5$ as described in our previous work (Kachabi et al., 2023). We assume a linear stress-strain relationship to close the system of equations, where the vessel stiffness, K (g/cm s^2) was analytically obtained by using the measured systolic pressure and area in the pressure-area relationship as written in equation (3):

$$P(x, t) = K \left(\sqrt{\frac{A(x, t)}{A_{dia}}} - 1 \right) + P_{dia}. \quad (3)$$

where $A_{dia} = \pi r_{dia}^2$ (cm^2) is the lumen area obtained from MR at the diastolic pressure P_{dia} (mmHg). K was fixed throughout the entire vasculature (both large and small arteries), as described in our previous work (Kachabi et al., 2023).

The PDE system in equations (1) and (2) requires boundary conditions at each vessel inlet and outlet, including at vessel junctions and terminal branches at the end of the MR imaging

domain. For the MPA inlet, we use a subject-specific measured time series flow as a boundary condition. At each vessel junction, we enforce flow conservation and pressure continuity (Kachabi et al., 2023). At the outlet of the terminal large arteries, we impose a synthetic vascular tree representative of the microvasculature using the structured tree model (Olufsen, 1999).

The structured tree attached to each terminal vessel is a construction of an asymmetric binary tree, where at each bifurcation the radii of the two offspring vessels are scaled by factors α and β ($0 < \beta < \alpha < 1$), respectively (Fig. 1). The network is truncated at a terminal radius, r_{min} , set to be 0.005 (cm) (Olufsen et al., 2012). The ST network can be formulated using the area ratio (ζ) and Murray exponent (η) (Olufsen, 1999)

$$\zeta = \frac{A_{d2}}{A_{d1}}, \quad r_p^\eta = r_{d1}^\eta + r_{d2}^\eta. \quad (4a,b)$$

The subscripts p , $d1$, and $d2$ represent the parent, larger offspring, and smaller offspring branch in the tree, respectively, and the offspring areas, A_{d2} and A_{d1} , correspond to the smaller and larger offspring vessels in each bifurcation. The area ratio ζ was determined using the MR imaging data and was calculated as the median value among all bifurcations across the large artery tree in all subjects, resulting in $\zeta = 0.6$. We note that η and ζ are related to α and β via the relationship (Olufsen, 1999)

$$\alpha = (1 + \zeta^{\eta/2})^{\frac{-1}{\eta}}, \quad \beta = \alpha\sqrt{\zeta}. \quad (5)$$

hence α and β are functions of η and ζ . For each vessel i in the ST, the reference radius is calculated by

$$r_i = r_{term} \cdot \alpha^g \cdot \beta^h. \quad (6)$$

where r_{term} is the radius of the terminal vessel to which the structured tree is attached, g is the degree of generation in the α path and h is the degree of generation in the β path. Also, for each given vessel i , the length of the vessel, l_i , is assumed to vary linearly with the vessel radius and is calculated by using the length-to-radius ratio (lrr):

$$l_i = r_i \cdot lrr. \quad (7)$$

As first noted by (Olufsen, 1999), the lrr modulates vascular impedance through the input impedance relationship:

$$\bar{Z}(0) = \frac{8\mu(r_0)lrr}{\pi r_0^3} + \bar{Z}(L). \quad (8)$$

where $\bar{Z}(0)$ and $\bar{Z}(L)$ are the mean (zero-frequency) impedances at the inlet and outlet of any terminal artery, $\mu(r_0)$ is the radius dependent viscosity, and r_0 is the reference radius (Colebank et al., 2021). The small vessels are also assumed to be linearly elastic, with the same stiffness as the large vessels.

Fluid dynamics in microvasculature are assumed to be viscous dominant, hence the nonlinear inertial terms are ignored in the momentum equation. This viscous-dominant system gives way to a periodic solution in the frequency domain, with angular frequencies $\omega_j = 2\pi j/T$ (radian / s) where T (s) is the length of the cardiac cycle, which is a wave equation (Olufsen et al., 2012). An analytical solution to the wave equation and flow conservation at junctions are used to construct an impedance relationship, where the total impedance of each ST, $Z_{tot}(\omega)$, is used as a boundary condition for the PDE system (see Olufsen (1999) for details).

Figure 1

2.4 Model parameters

The model includes two different sets of parameters. The constant fluid parameters are fixed based on literature, such as μ and ρ , or obtained from data, like ζ , K , and T , for each individual subject. A different set of parameters describing the microvasculature are inferred to match each subject's hemodynamic data, including the Murray exponent (η), and length to radius ratio (lrr). Since CTEPH is a heterogeneous disease that can affect each side of the lung differently, we used independent η and lrr parameters for the left and right lungs. This also parallels findings in Mulchrone et al., which identified an unequal number of microspheres in the left and right lung. In total, our parameter set to be inferred is four-dimensional, comprised of $\theta = \{\eta_L, \eta_R, lrr_L, lrr_R\}$, where L and R denote the left and right lung parameters.

2.5 Emulation

We overcome the computational burden of using our expensive PDE simulator by using GP emulation. GPs are beneficial in comparison to other emulators because they are more robust at capturing model dynamics using smaller datasets for training (Paun & Husmeier, 2021). Briefly, a stochastic process, $f = f(\theta)$, is defined as a GP if the finite collection of random variables ($f(\theta_1), \dots, f(\theta_n)$) are jointly normal for inputs $\theta_i \in \mathbb{R}^p$, where $i = 1, \dots, n$ are the realizations and p is the parameter dimensionality. We write the GP as $f \sim GP(\mathbf{m}, \mathbf{K})$, where \mathbf{m} is the mean function and $\mathbf{K} = [k(\theta_i, \theta_j)]_{i,j=1}^n$ is the $n \times n$ variance-covariance matrix of f based on the kernel function $k(\theta_i, \theta_j)$. In GP models, the input Θ an ($n \times d$ matrix) are mapped to outputs $\mathbf{y} = (y_1, \dots, y_n)$ (an n -vector) through latent noiseless functions \mathbf{f} (Bonilla et al., 2008.; Paun & Husmeier, 2021; Rasmussen & Williams, 2006).

We trained a GP model on 3,000 datasets from the PDE simulator with different parameter combinations, $\boldsymbol{\theta}_{\text{Sampling}} = \{\eta_L, lrr_L, \eta_R, lrr_R\}$, using a Latin hypercube design. Table 1 presents the upper and lower bounds selected for the datasets. To obtain the intervals for sampling, we combined calculations from the large vessel imaging data and previous literature values (Keelan & Hague, 2021; Olufsen et al., 2012; Uylings, 1977). For the Murray exponent (η) value, we solved equation (4b) for η at each bifurcation for each subject using a Newton-Raphson minimization in MATLAB (Mathworks, Nantick MA). By aggregating the η values across various bifurcations and subjects, we initially obtained a range of [0.5,4]. We narrowed this interval to [1.5,3] based on physiological considerations and the operational limits of our 1D fluid model (Murray, 1926; Olufsen, 1999). For the parameter lrr , the range we obtained from data in the large vessels was [0.1,44]. Olufsen et al. (2012) suggested that lrr , values can reach up to 50 for both systemic and pulmonary circulation. To accommodate this and provide a broader interval, we extended the range to [2.5,70].

The simulator outputs include four different time-varying signals: MPA pressure, LPA and RPA flows, and MPA area, making the final output dimension a 35 x 4 matrix. To reduce computational complexity that would be attributed to multitask learning for our vectorized outputs, we applied principal component analysis (PCA) to the simulator outputs. The PCA representation of the model outputs is given by

$$\mathbf{y}(\boldsymbol{\theta}, \mathbf{t}) = \bar{\mathbf{y}} + \sum_{i=1}^{n_{PCA}} c_i(\boldsymbol{\theta}) \boldsymbol{\xi}_i(\mathbf{t}) + \boldsymbol{\varepsilon}_i(\mathbf{t}). \quad (9)$$

where n_{PCA} is the number of PCA terms, $\bar{\mathbf{y}}$ is the mean of the simulator outputs \mathbf{y} , $\boldsymbol{\xi}_i$ are the eigenvectors corresponding to the sample covariance matrix of the data, $c_i(\boldsymbol{\theta})$ are the principal component scores, and $\boldsymbol{\varepsilon}_i(\boldsymbol{\theta}, \mathbf{t})$ represents the error in the PCA approximation. Since the principal components of the outputs are independent, we emulate the PCA scores, $c_i(\boldsymbol{\theta})$ using independent GPs (Bonilla et al., 2008.). We employed min-max scaling for both the parameter inputs and simulator outputs to account for differences in magnitudes and ensure robust emulator building (Singh & Singh, 2020). We used a zero mean GP function, similar to previous work (Paun & Husmeier, 2021). We performed PCA on each subject's simulator data set individually and fixed the number of principal components based on maximum required components to capture more than 99.9% of the original variance across all datasets. This resulted in $n_{PCA} = 20$ principal components, reducing the original dimensionality down from 140, and thus emulate the PCA data using 20 independent GPs for each $c_i(\boldsymbol{\theta})$ with a Matérn covariance kernel ($\nu = 5/2$).

Table 1 Parameter bounds for sampling.

Parameter	η_L	lrr_L	η_R	lrr_L
Range	1.5 – 3	2 – 70	1.5 – 3	2 – 70

To train the GPs, we minimize the negative log likelihood of the model, calculated using the marginal log likelihood of the observed data, using the Adam optimizer with a learning rate of 0.1. We monitor convergence across 1,000 iterations. All GP implementation and training was done in the GPytorch infrastructure (Gardner et al., 2018.) and is available at <https://github.com/AmirrezaKachabi>.

2.6 Inverse problem and model calibration

We use the collection of subject-specific measurements, $\mathbf{y} = \{p_{sys}^{MPA}, p_{dia}^{MPA}, \mathbf{q}^{LPA}, \mathbf{q}^{RPA}, \boldsymbol{\varepsilon}^{MPA}\}$, for the inverse problem. Here, $\boldsymbol{\varepsilon}^{MPA}$ is the MPA relative area change obtained from dynamic area using $\varepsilon(t) = \frac{A(t) - A_{dia}}{A_{dia}}$. We use relative area change instead of dynamic area to account for the constant use of the baseline geometry in each subject. Further, $\varepsilon(t)$ is suggested to be a non-invasive measure of proximal arterial stiffening and a predictor of mortality in PH (Gan et al., 2007). The relative area change signals were converted to percentage values for the inverse problem.

We use a Bayesian framework for parameter inference. We assume the parameters are random variables, where the prior parameter distributions and likelihood function are used to sample from the approximate posterior distribution conditioned on the observed data. This gives rise to Bayes' formula:

$$P(\boldsymbol{\theta}|\mathbf{y}) = \frac{P(\mathbf{y}|\boldsymbol{\theta})P(\boldsymbol{\theta})}{\int P(\mathbf{y}|\boldsymbol{\theta})P(\boldsymbol{\theta})d\boldsymbol{\theta}}. \quad (10)$$

Given measured data \mathbf{y} , $P(\mathbf{y}|\boldsymbol{\theta}) = \mathcal{L}(\mathbf{y}|\boldsymbol{\theta})$ is the likelihood function, and $P(\boldsymbol{\theta})$ is the prior distribution for the parameters. The term $\int P(\mathbf{y}|\boldsymbol{\theta})P(\boldsymbol{\theta})d\boldsymbol{\theta}$ is the evidence or the normalization factor, which is approximated here using Markov chain Monte Carlo (MCMC). In place of the true likelihood using our PDE system, we use the GP emulator.

We consider two different prior distributions to investigate its impact on the posterior densities. First, we use Gaussian prior distributions derived from the median and standard deviation of the large vessel parameters across all subjects over the physiological ranges defined in Table 1. Specifically, we assume that the priors are $\eta \sim \mathcal{N}(2.13, 0.37)$ and $lrr \sim \mathcal{N}(10.7, 8)$. For comparison, we also use a uniform prior over the plausible parameter space defined in Table 1. We prescribe different magnitudes of measurement error to each of the four measurement modalities, giving the likelihood function:

$$\mathcal{L}(\mathbf{y}|\boldsymbol{\theta}) = \frac{1}{(2\pi)^{N_t/2}} \det(\boldsymbol{\Sigma}_y)^{-1/2} \exp\left(-\frac{1}{2}(\mathbf{y} - \widetilde{\mathbf{m}}(\boldsymbol{\theta}))^\top \boldsymbol{\Sigma}_y^{-1}(\mathbf{y} - \widetilde{\mathbf{m}}(\boldsymbol{\theta}))\right). \quad (11)$$

The likelihood includes $N_t = 107$ data points corresponding to the original data, \mathbf{y} , $\bar{\mathbf{m}}(\boldsymbol{\theta})$ is the inverse PCA transformed GP model predictions, and the measurement covariance $\boldsymbol{\Sigma}_y \in \mathbb{R}^{N_t \times N_t}$ is a diagonal matrix containing the measurement error for each data source. The measurement error values in $\boldsymbol{\Sigma}_y$ updated according to an inverse-gamma distribution (Smith, 2024). We sample from the approximate posterior using the delayed rejection adaptive Metropolis (DRAM) algorithm in the pymcmcstat package (Miles, 2019). We run DRAM for 10,000 iterations, with the first 2,000 iterations treated as the burn-in phase. To determine the convergence of the MCMC chains, we use the Geweke test, which compares the first 10% and last 50% of the chain for significant differences in the mean and computes a p-value from a Z-statistic (Smith, 2024). We use the last 2,000 samples to propagate uncertainties forward through the model and construct credible and prediction intervals for the model output. A summary of the entire process can be found in Fig. 2.

Figure 2

2.7 Statistical analysis

To compare the marginal posteriors between baseline and CTEPH and with different priors, we used the Kolmogorov-Smirnov (KS) test with a p-value < 0.05 considered significant. We used the Mann-Whitney U test to compare the posterior distributions of microvascular parameters of each subject before and after CTEPH. Finally, we used the Pearson correlation coefficient performed based on relative changes between the model outputs from baseline to CTEPH to quantify relationships between model parameters and predictions. We used the flow split ratio (q_r), calculated using the formula below, and relative changes in mean pulmonary arterial pressure (mPAP) as the measures of disease severity to investigate the correlation with microvasculature parameters:

$$q_r = \frac{\bar{q}_m^{LPA}}{\bar{q}_m^{LPA} + \bar{q}_m^{RPA}}. \quad (12)$$

where \bar{q}_m denotes the time average flow derived from the model.

3 Results

3.1 Emulation accuracy

We reserved 5% of each subject's PDE simulator data as test data to assess emulator accuracy. We calculated the log mean squared error (MSE) for each output quantity (i.e., pressure, flows, and area) in both baseline and CTEPH subjects. We denote subjects 1-5 as S1-S5 respectively. Note that each data source has different units and order of magnitude.

Figure 3

As shown in Fig. 3(a), all subjects (S1-S5) show similar accuracy in pressure, except for S1 and S5 in baseline, and S1 in CTEPH, which have a lower median log MSE. The same trend exists for the area predictions, as provided in Fig. 3(b). This behavior can be attributed to the direct relationship between pressure and area. Due to the correlation between the flows for a given simulation, the median log MSE for LPA and RPA flow are similar in magnitude across most cases as shown in Fig.3 (c-d). We note that S1 has the largest flow MSE outliers among the subjects especially at baseline. In general, median MSE values are lower in the LPA than the RPA, reflecting better accuracy of the emulator in the left branch. We note that there is variability among subjects in the accuracy of the emulator across output types. On average, there is reasonable agreement between the GP and PDE test data in both baseline and CTEPH conditions.

3.2 Model calibration

Figures 4 and 5 illustrate the four measured data sources, along with calibrated GP predictions at the posterior mean, in baseline and CTEPH respectively. We also show 95% credible and prediction intervals, derived from the last 2,000 simulations, for all subjects. The agreement between the data and the GP varies among the subjects. Model predictions show excellent agreement with the measured data in S1 (Fig. 4(a)) and S4 (Fig. 4(c)). For S2 (Fig. 4(b)), LPA and RPA flows align well with the time-series data, while the GP predictions for systolic pressure and maximum strain are notably higher than the measured data. Model predictions in S4 (Fig. 4(d)) agree well with the data also, with only a slight underestimation of maximum LPA flow and systolic pressure. As depicted in Fig. 4(e), in S5 the GP model performs exceptionally well for pressure and flows, with only a slight mismatch in maximum strain, which is covered by the prediction interval.

Figure 4

Similar to baseline, there is variability among CTEPH subjects in the agreement between the data and the GP, with generally less agreement compared to the baseline cases (Fig. 5). Systolic pressures match well for S3 (Fig. 5(c)), while for the other subjects the GP predictions are larger in magnitude than both the systolic and diastolic data. For the LPA flow in S1, the model provided an excellent fit, while for the other subjects there are some mismatches in flow magnitude as shown in Fig. 5(a). However, the GP can emulate flow waveform shapes reasonably well in both systole and diastole. Predictions of RPA flow match well in S1, S3, and S4 (Fig. 5(d)), while there are slight mismatches for S2 and S5 (Fig. 5(e)). For strain, the fits for S3 and S4 agree well with the data, while the GP model overestimated the maximum strain in S1, S2, and S5.

Figure 5

3.3 Marginal posterior densities

Figure 6 shows the marginal posterior densities for all subjects in both baseline and CTEPH conditions. We provide the baseline (blue) and CTEPH (red) posteriors for each subject in the same plot for each parameter. The posterior distributions of all model parameters were found to be significantly different (p -value < 0.005) between baseline and CTEPH using the KS test. However, Fig. 6 qualitatively suggests that for certain subjects, this difference is not substantial. For example, η_L in S1 or η_R in S2, S3, and S5, as well as lrr_R in S3 appear similar. Furthermore, the Mann-Whitney U test also supported that CTEPH significantly altered the parameter distributions (p -value < 0.005). For the left lung, CTEPH significantly reduced η_L across all subjects and increased lrr_L in all subjects except S3. In the right lung, the results were heterogeneous: η_R decreased in subjects S1 and S5 but increased in S2, S3, and S4, while lrr_R significantly decreased in S1 and S3 and significantly increased in S2, S4, and S5

Figure 6

3.4 Effect of Prior Distribution

The results in Fig. 6 were obtained under the assumption of a data-driven, Gaussian prior based on values obtained from MR data. To identify the effects of this assumption, Fig. 7 shows the marginal parameter posteriors using either data driven, Gaussian priors (solid lines) or using uniform priors on the plausible parameter range (dashed lines) in baseline. Results are obtained using the same MCMC routine described earlier. In S1, the posterior densities for both η_L, η_R were slightly shifted to the left, with minimal impact on either lrr . In S2, the prior had no influence on η_L, lrr_L , or lrr_R , but it made the posterior for η_R more unimodal. S3 was the only case in which the informative prior affected all parameter posteriors at baseline, shifting them to the left. In S4, the informative prior had almost no impact on the posteriors of other parameters but successfully mitigated the long tail observed in the posterior of η_R . Similarly, in S5, the informative prior did not affect any of the marginal posteriors.

Figure 7

Figure 8 shows how the prior density impacted these subjects in CTEPH. The Gaussian prior increased the posterior samples of the left lung parameters while decreasing the right lung parameters in S1 and S4. In S2, the shape of the posteriors was mostly affected, with the mode remaining almost unchanged. In S3, the informative prior had no impact on the left lung

parameters, but it shifted the right lung parameters to toward smaller values. In S5, all four parameters shifted to the right. These results suggest that inference using the CTEPH data was more sensitive to the choice of prior.

Figure 8

3.5 Parameter correlation

To analyze the microvasculature parameters and their changes with disease severity, we performed Pearson correlation analysis. Correlations values are shown in Fig. 9, with those above 0.80 and below -0.80 highlighted as strong correlations. We found strong positive correlations between q_r (see equation (10)) and left lung parameters (η_L and lrr_L) while for the mPAP, we noticed a strong positive relationship just with lrr_L . In contrast, the correlations with the η_R were relatively weak.

Figure 9

4 Discussion

In this study, we emulated a 1D pulmonary circulation model using GPs. Our aim was to computationally investigate the impacts of CTEPH on the microvasculature, a domain that is challenging to study clinically or preclinically using current imaging equipment. By employing GPs as an emulator for the expensive PDE model, we were able to estimate model parameters describing the microvasculature using Bayesian inference. This approach allowed us to quantify uncertainties in model parameters and emulated outputs, and offers valuable insights, particularly when working with limited and noisy data.

4.1 Gaussian Process Emulation

Statistical emulation modeling is a widely used approach to reduce complexity and enhance computational efficiency in mathematical models. The choice of an emulator depends on the characteristics of the dataset and the requirements of the mathematical model. For example, Paun et al. (2025) conducted a comparative analysis of GPs and PCEs using the same 1D fluid dynamics model with two different terminal boundary conditions for both forward and inverse problems. They reported that GPs consistently performed slightly better than PCEs in every comparison. In this work, we used GPs due to its advantages over other methods and its relative flexibility in function approximation. GPs typically require smaller datasets for effective training; for instance, we used 3,000 samples for training, whereas neural network architectures can require substantially more samples for the training process (Myren & Lawrence, 2021).

Emulating time-series data can require additional GP kernels to account for both parameter and time-dependent correlations of the simulator (Paun et al., 2024). Several studies have overcome this by combining GPs with PCA-based dimensionality reduction techniques (N.

Lawrence, 2005; N. D. Lawrence, 2004). Previous studies (Paun et al., 2025.; Paun et al., 2024; Pratola & Higdon, 2016) demonstrated that applying PCA to the output space does not have a significant effect on the accuracy of model predictions. Therefore, for our problem, we used PCA representations of our outputs to reduce the output dimensions from 140 to 20, thereby speeding up the training process. This also provides consistent theoretical links between the use of independent GPs with independent PCA components. The GP accuracy for predicting test data varies among the subjects in baseline and CTEPH. As shown in Fig. 3 (a-b) for pressure and area and Fig. 3 (c-d) for flows, the trends are similar among the subjects. In certain cases, some observations cause the outliers to reach a $\log(\text{MSE}) = 10^{-1}$. However, on average, the $\log(\text{MSE})$ remains relatively small among different cases. We note that some of the poor fits to test data are attributed to specific combinations of parameters that generate non-physiological signals in both magnitude and shape, such as unrealistic pressures (>120 mmHg) or large portions of negative flow in the proximal arteries. These results suggest that, in general, emulations align with the simulations across all four data sources, especially in the parameter domain near the inferred parameters.

4.2 Parameter inference

The emulator enabled time-efficient model calibration using real measured data while quantifying uncertainties that are necessary in the clinical setting. Several studies have trained GP emulators to handle parameter estimation problems (Bai et al., 2024; Teckentrup, 2020). In the systemic circulation, several studies have used GPs to reduce computation time for quantifying uncertainties in their model predictions (Ashtiani et al., 2024; Yin et al., 2019). In the context of pulmonary blood flow simulation, Paun and Husmeier (2021) trained a GP for a 1D fluid dynamics model of pulmonary arteries in mice using Windkessel boundary conditions. They identified scaling factors for the Windkessel parameters through Bayesian inference with measured pressure signals. In another study, Paun et al. (2025) utilized the same 1D fluid dynamics model with both Windkessel and structured tree boundary conditions. After training both GP and polynomial chaos expansions as emulators, they applied a frequentist approach to estimate model parameters using only a pressure signal as data. Choosing the set of parameters for inference is problem specific. (Paun et al., (2021) used the same 1D fluid model with Windkessel boundary conditions, aiming to determine whether model recalibration at a high degree of accuracy is feasible based on blood flow measurements alone, without the need for another CT scan. Their parameter sets included Windkessel parameters, and they also attempted to infer vessel wall material properties and vasodilation effects. In our study, we used a 1D fluid dynamics model with structured tree boundary conditions to model microvascular disease. We accounted for the heterogeneous pattern of CTEPH by separating left and right lung parameters. We also fixed the vessel wall stiffness using a simple pressure-area relationship (Kachabi et al., 2023).

We applied Bayesian inference with the emulator to infer the model parameters and capture uncertainties in the model parameters and outputs. Since we had four different data sources, each recorded using different modalities, we defined our likelihood functions such that each source included a separate noise-variance term, instead of combining them into a single likelihood function with a common noise term (Kachabi et al., 2024; Paun et al., 2024). Overall, the quality of fits was better with baseline data compared to CTEPH data, as shown in in Fig. 4 and Fig. 5, respectively. One possible reason for this discrepancy is that although the dogs were of the same breed, age, and sex, they reacted differently during the development of CTEPH. For example, some cases required $\sim 30,000$ microspheres while others needed $\sim 60,000$ microspheres to reach CTEPH conditions (Mulchrone et al., 2019). Additionally, we fixed the geometry to capture the impact of CTEPH on the structured tree parameters, which represent the microvasculature. However, comparing imaging data between subjects from baseline to CTEPH reveals differences in the larger vasculature, as reported by our group previously (Kachabi et al., 2023) This suggests that CTEPH may lead to changes in both proximal, large arteries as well as the microvasculature

Blood pressure is a critical factor, as PH is diagnosed based on elevated pressure levels. Consequently, most studies have calibrated their models using measured pressure signals (Paun et al., 2018; Qureshi et al., 2019; Zambrano et al., 2018). In our study, the pressure measurements were limited to systolic and diastolic points, and we did not have access to the full pressure waveform. In a recent study, Taylor-Lapole et al., (2024) employed a similar 1D fluid dynamics framework for the systemic circulation using structured tree boundary conditions. The patient data used for model calibration included systolic and diastolic pressure, along with four dynamic flow signals. Their model predictions revealed wider prediction intervals for pressure compared to flow. Similarly, in our study, we observed larger prediction intervals for pressure relative to other data sources, particularly in cases where the pressure fit was less accurate. Overall, almost all subjects showed reasonable agreement between the data and model predictions, including the prediction intervals, in the baseline condition. The exception was S2, which could be attributed to its unusually small, non-physiological pulse pressure (10 mmHg) compared to the other subjects. In the CTEPH condition, the model predictions overestimated the pressure signal for four of the subjects, with the exception of S3. This could be due to the minimal change in the measured pressure signal for S3 between the baseline and CTEPH conditions. Furthermore, as mentioned earlier, we fixed the vessel stiffness, which has a direct impact on the pulse pressure. Though we could infer the stiffness parameter (Qureshi et al., 2019), this makes the inverse problem more complex and draws attention away from the sole effects of microvasculature parameters. We also note that we obtain nearly uniform marginal posterior densities for stiffness (results not shown) when it is inferred, suggesting that inferring stiffness with limited pressure data leads to identifiability issues.

As shown in Fig. 4, both LPA and RPA flow fits were reasonable in baseline, except for the LPA in S4. These discrepancies can be attributed to the significantly higher proportion of negative flow measured in the LPA for this subject compared to others. Fit qualities varied in CTEPH, even

though the model captured the general rise and fall of the measured waveforms (Fig. 5). This discrepancy could be attributed to the impacts of CTEPH on the large vessels, since the large vasculature was kept unchanged from baseline to CTEPH. These effects were particularly evident in the LPA fits, which are likely attributed to worse remodeling in the left lung (Mulchrone et al 2019).

Since there is a direct relationship between pressure and area in our model, the quality of the strain fits to the data follow a similar trend to the pressure fits. In the baseline condition, both pressure and strain fits are reasonable for four out of five subjects. Again, S2 shows the worst fit (Fig. 4), likely due to the very small pulse pressure. We note that pulse pressure is linked to stiffness, so having a small pulse pressure and high strain at the same time is unusual, as small strain usually indicates higher stiffness (Wei et al., 2022). This may be why the emulator is unable to capture such a set of measurement signals. CTEPH results in Fig. 5 showed a similar trend in strain and pressure fits. Interestingly, despite the overestimation of pressure in S4, the emulated strain is nearly identical to the data.

4.3 CTEPH effects on the model parameters

We sought to assess the impact of CTEPH on microvascular parameters in the model. The microvasculature is believed to involve more complex mechanisms in PH progression compared to the large vessels (Fedullo et al., 2000.; Hoeper et al., 2006). Previous computational modeling studies (Kachabi et al., 2023; Colebank et al., 2021; Spazzapan et al., 2018; Tsubata et al., 2023) investigated CTEPH and hemodynamic changes in large arteries; however, none of them have explored microvascular disease in a patient-specific, CTEPH context. To model the microvasculature, we used the structured tree boundary conditions as previously used in the pulmonary circulation (Bartolo et al., 2022; Paun et al., 2024.; Paun et al., 2025).

The Murray exponent, η , specifies how the diameter varies across each bifurcation (Olufsen et al., 2000). This relationship is derived based on optimizing the balance between the energy required to pump blood (pressure-flow energy) and the metabolic energy (Murray, 1926). Previous studies (Olufsen, 1999; Olufsen et al., 2012; Qureshi et al., 2014) used a range of η values for different flow regimes, with $\eta = 3$ being optimal for laminar flow and $\eta = 2.33$ for turbulent flow. Nakamura et al. Nakamura & Awa (2014) review a variety of studies that examine the Murray exponent across different organs and species, reporting values ranging from approximately 2.1 to 3.5 in systemic arterial trees, while noting a broader range in the pulmonary vasculature. As mentioned earlier, we set the η range to [1.5,3] by combining imaging data from large arteries and prior fluid dynamics-based reasoning (Olufsen et al., 2000).

Theoretical analyses have demonstrated that the Murray exponent decreases curvilinearly with increasing Reynolds number (for inertial effects) and increasing Womersley number (for unsteady effects) (Shumal et al., 2024; Uylings, 1977). We can interpret our results from Fig. 6 in

the following context: in the left lung, we observed a significant reduction in the Murray exponent from baseline to CTEPH. Since we also observed a decrease in LPA flow, the Reynolds and Womersley numbers will only increase when there is a decrease in diameter. Hence, smaller Murray exponents under low flow conditions imply a reduction in small vessel diameter. This finding aligns with previous reports (Mulchrone et al., 2019) highlighting more severe vascular obstruction in the left lung compared to the right lung and likely left-lung remodeling. The Murray exponent in the right lung exhibited a heterogeneous pattern, which may be attributed to less pronounced disease severity compared to the left lung. The computational study by Kozitza et al (2024) also concluded that stenoses and obstructed flow to the left lung likely led to moderate decreases in radii due to hypoperfusion.

As shown in Fig. 6, the lrr_L value increased in all subjects from baseline to CTEPH, except S3, which may be attributed to only a slight pressure change from baseline to CTEPH in this subject. The observed increase in the length-to-radius ratio is likely due to elevated vascular resistance caused by a decrease in vessel radius relative to vessel length following the development of CTEPH. Consistent with the findings for the Murray exponent, this alteration was more pronounced in the left lung, further supporting the heterogeneous nature of disease severity between the two lungs. In addition, the lrr value modulates the mean impedance, $Z(0)$, of the structured tree, thus reflecting increased resistance in the left lung due to CTEPH.

Variability in pulmonary blood flow serves as an early marker of lung disease or susceptibility to such conditions (Clark & Tawhai, 2018). Yang et al (2018) used 3D fluid dynamics simulation to evaluate the hemodynamic effects of pulmonary artery reconstruction in patients with Alagille syndrome and peripheral pulmonary stenosis, reporting that flow split in the pulmonary circulation can be an indicator of disease risk. In this study, we used the flow split index, q_r , as an indicator of microvascular disease severity. As illustrated in Fig. 9, q_r exhibits a strong positive relationship with both left lung parameters. This relationship can be attributed to the impact of severe obstruction in the left lung, which significantly influenced both parameters. Moreover, the positive correlation between mPAP and lrr_R can be attributed to the remodeling that occurred in the right lung (the less obstructive lung), which experienced an increase in flow. The increase in flow led to higher wall shear stress, which is suggested to play a role in vascular enlargement and elongation (Hofer et al., 2013). This remodeling increases impedance, requiring higher pressure to sustain flow. These findings highlight the model's ability to capture and reflect disease severity effectively.

4.4 Effect of Prior Distribution

In Bayesian inference, an overly informative prior can disproportionately affect posterior estimates and subsequent conclusions about the parameters (Depaoli et al., 2020; Morita et al., 2010). In contrast, the biggest benefit of Bayesian inference is the ability to use prior information. Therefore, it is crucial to use prior information carefully to avoid introducing unnecessary bias into the results.

In our study, we use imaging data to inform the prior distributions for inference. The physiological hypothesis is that, overall, these parameters should follow a similar trend across large and small vessels. We compared solutions to the inverse problem using uniform priors and data-informed priors as shown in Fig. 7 and Fig. 8 for both baseline and CTEPH, respectively. Overall, the data-informed prior had a greater influence on the CTEPH cases. This can be attributed to the fact that the prior information was derived from imaging data corresponding to the baseline condition and fixed in both situations. Furthermore, the use of informative priors transformed some marginal posterior distributions with long tails into more concentrated distributions, particularly in S2 and S5 for CTEPH. The sensitivity of left and right lung parameters to the prior distribution were divergent: the left lung parameters almost always shifted to the right, while right lung parameters exhibited variable behavior, including mostly leftward shifts (S1, S3, S4) and one rightward shift (S5).

5 Limitations

Our study has several limitations. First, time-varying pressure signals were not captured during data collection, and instead, only systolic and diastolic data was available. Calibrating the model using only systolic and diastolic pressures made the model calibration process more difficult and having a dynamic pressure signal would simplify the inverse problem and result in smaller prediction intervals for the pressure signal (Paun et al., 2020). Second, we parameterized our model so that the entire left lung and right lung were described by lobe-specific parameters. Ideally, each vessel could have its own parameters, but this would make inference exceedingly difficult and likely introduce parameter identifiability issues (Paun et al., 2020). Third, since our focus was on modeling microvascular disease in CTEPH, we fixed the geometry at baseline and inferred the parameters for both baseline and CTEPH. By doing so, we ignored alterations in the larger vessels after microsphere injection, which is not entirely realistic. Fourth, due to limited data, we applied a fixed set of assumptions, such as the area ratio and informative priors, derived from imaging data across all subjects. Incorporating subject-specific values for these parameters would enhance the study by making it more tailored to individual subjects, as each one ultimately has a unique vascular network. Finally, our sample size was small, making it difficult to draw solid conclusions, particularly in correlation analysis. A larger sample size would provide better insights and lead to a stronger understanding of how simulated quantities and model parameters correlate with disease severity.

6 Conclusion

We combined emulation with a 1D fluid dynamics model of the pulmonary circulation to efficiently estimate microvascular model parameters and their uncertainty. We reduced the computation time of the problem using Gaussian processes and utilized actual experimental data

from a previous animal model of the condition in a Bayesian inverse problem setting. We successfully calibrated the model against measured data for both baseline and CTEPH cases with reasonable accuracy, reducing the process time from the order of months without emulation to just three hours per animal using GPs. This efficient calibration method, which also quantifies the uncertainty in subject-specific predictions, can provide deeper clinical insights and greater confidence in making patient-specific decisions. We also demonstrated that CTEPH gives rise to heterogeneous disease severity in the microvasculature and correlates with the inferred model parameters. Ultimately, this approach serves as a crucial step toward better understanding the complex mechanisms of microvascular disease in CTEPH, laying the foundation for future synergistic studies aimed at developing more precise computational diagnostic tools and targeted interventions tailored to individuals with CTEPH.

Acknowledgements

This work was funded by the National Institutes of Health NIBIB grants R01HL154624 (NCC) and R01 HL147590 (NCC). M.J.C. was supported TL1 TR001415 through the National Center for Research Resources and the National Center for Advancing Translational Sciences, National Institutes of Health. The content is solely the responsibility of the authors and does not necessarily represent the official views of the NIH.

REFERENCES

- Ashtiani, S. Z., Sarabian, M., Laksari, K., & Babaee, H. (2024). Reconstructing blood flow in data-poor regimes: a vasculature network kernel for Gaussian process regression. *Journal of the Royal Society Interface*, 21(217). <https://doi.org/10.1098/rsif.2024.0194>
- Bai, T., Teckentrup, A. L., & Zygalakis, K. C. (2024). Gaussian processes for Bayesian inverse problems associated with linear partial differential equations. *Statistics and Computing*, 34(4). <https://doi.org/10.1007/s11222-024-10452-2>
- Bartolo, M. A., Qureshi, M. U., Colebank, M. J., Chesler, N. C., & Olufsen, M. S. (2022). Numerical predictions of shear stress and cyclic stretch in pulmonary hypertension due to left heart failure. *Biomechanics and Modeling in Mechanobiology*, 21(1), 363–381. <https://doi.org/10.1007/s10237-021-01538-1>
- Beliaev, D., & Smirnov, S. (Eds.). (2023). *International Congress of Mathematicians* (Vol. 4). EMS Press. <https://doi.org/10.4171/icm2022-4>
- Bonilla E, Chai KM, Williams C. Multi-task Gaussian process prediction. In: Proceedings of the 20th annual conference of neural information processing systems. 2008. 153–60
- Clark, A. R., & Tawhai, M. H. (2018). Temporal and spatial heterogeneity in pulmonary perfusion: A mathematical model to predict interactions between macro-and micro-vessels in health and disease. *ANZIAM Journal*, 59(4), 562–580. <https://doi.org/10.1017/S1446181118000111>

- Colebank, M. J., Qureshi, M. U., Rajagopal, S., Krasuski, R. A., & Olufsen, M. S. (2021). *A multiscale model of vascular function in chronic thromboembolic pulmonary hypertension*. <https://doi.org/10.1152/ajpheart.00086.2021>
- Conti, S., & O'Hagan, A. (2010). Bayesian emulation of complex multi-output and dynamic computer models. *Journal of Statistical Planning and Inference*, *140*(3), 640–651. <https://doi.org/10.1016/j.jspi.2009.08.006>
- Depaoli, S., Winter, S. D., & Visser, M. (2020). The Importance of Prior Sensitivity Analysis in Bayesian Statistics: Demonstrations Using an Interactive Shiny App. *Frontiers in Psychology*, *11*. <https://doi.org/10.3389/fpsyg.2020.608045>
- Di Achille, P., Harouni, A., Khamzin, S., Solovyova, O., Rice, J. J., & Gurev, V. (2018). Gaussian process regressions for inverse problems and parameter searches in models of ventricular mechanics. *Frontiers in Physiology*, *9*(AUG). <https://doi.org/10.3389/fphys.2018.01002>
- Fedullo, P. F., Rubin, L. J., Kerr, K. M., Auger, W. R., & Channick, R. N. (2000). The natural history of acute and chronic thromboembolic disease: the search for the missing link. *European Respiratory Journal*, *15*(3), 435–436. <https://doi.org/10.1034/j.1399-3003.2000.15.01.x>
- Galiè, N., & Kim, N. H. S. (2006). Pulmonary microvascular disease in chronic thromboembolic pulmonary hypertension. *Proceedings of the American Thoracic Society*, *3*(7), 571–576. <https://doi.org/10.1513/pats.200605-113LR>
- Gan, C. T. J., Lankhaar, J. W., Westerhof, N., Marcus, J. T., Becker, A., Twisk, J. W. R., Boonstra, A., Postmus, P. E., & Vonk-Noordegraaf, A. (2007). Noninvasively assessed pulmonary artery stiffness predicts mortality in pulmonary arterial hypertension. *Chest*, *132*(6), 1906–1912. <https://doi.org/10.1378/chest.07-1246>
- Gardner, J. R., Pleiss, G., Bindel, D., Weinberger, K. Q., & Wilson, A. G. (2018). *GPyTorch: Blackbox Matrix-Matrix Gaussian Process Inference with GPU Acceleration*. <http://arxiv.org/abs/1809.11165>
- Gerges, C., Gerges, M., Friewald, R., Fesler, P., Dorfmüller, P., Sharma, S., Karlocai, K., Skoro-Sajer, N., Jakowitsch, J., Moser, B., Taghavi, S., Klepetko, W., & Lang, I. M. (2020). Microvascular Disease in Chronic Thromboembolic Pulmonary Hypertension: Hemodynamic Phenotyping and Histomorphometric Assessment. *Circulation*, *141*(5), 376–386. <https://doi.org/10.1161/CIRCULATIONAHA.119.041515>
- Ghafariasl, P., Mahmoudan, A., Mohammadi, M., Nazarpour, A., Hoseinzadeh, S., Fathali, M., Chang, S., Zeinalnezhad, M., & Garcia, D. A. (2024). Neural network-based surrogate modeling and optimization of a multigeneration system. *Applied Energy*, *364*. <https://doi.org/10.1016/j.apenergy.2024.123130>
- Hofer, I. E., Den Adel, B., & Daemen, M. J. A. P. (2013). Biomechanical factors as triggers of vascular growth. In *Cardiovascular Research* (Vol. 99, Issue 2, pp. 276–283). <https://doi.org/10.1093/cvr/cvt089>
- Hooper, M. M., Mayer, E., Simonneau, G., & Rubin, L. J. (2006). Chronic thromboembolic pulmonary hypertension. In *Circulation* (Vol. 113, Issue 16, pp. 2011–2020). <https://doi.org/10.1161/CIRCULATIONAHA.105.602565>

- Hu, Z., Wang, H., & Zhou, Q. (2024). A MCMC method based on surrogate model and Gaussian process parameterization for infinite Bayesian PDE inversion. *Journal of Computational Physics*, 507. <https://doi.org/10.1016/j.jcp.2024.112970>
- Huang, Y., Liu, D., & Wu, H. (2006). Hierarchical Bayesian Methods for Estimation of Parameters in a Longitudinal HIV Dynamic System. *Biometrics*, 62(2), 413–423. <https://doi.org/10.1111/j.1541-0420.2005.00447.x>
- Kachabi, A., Colebank, M. J., & Chesler, N. C. (2023). Subject-specific one-dimensional fluid dynamics model of chronic thromboembolic pulmonary hypertension. *Biomechanics and Modeling in Mechanobiology*. <https://doi.org/10.1007/s10237-023-01786-3>
- Kachabi, A., Colebank, M. J., Correa, S. A., & Chesler, N. C. (2024). *Markov Chain Monte Carlo with Gaussian Process Emulation for a 1D Hemodynamics Model of CTEPH*. 8th International Conference on Computational and Mathematical Biomedical Engineering (Vol. 2, pp. 449-452). <http://arxiv.org/abs/2406.01599>
- Kamiya, A., & Togawa, T. (1980). *Adaptive regulation of wall shear stress to flow change in the canine carotid artery*.
- Keelan, J., & Hague, J. P. (2021). The role of vascular complexity on optimal junction exponents. *Scientific Reports*, 11(1), 5408. <https://doi.org/10.1038/s41598-021-84432-1>
- Kozitza, C. J., Colebank, M. J., Gonzalez-Pereira, J. P., Chesler, N. C., Lamers, L., Roldán-Alzate, A., & Witzenburg, C. M. (2024). Estimating pulmonary arterial remodeling via an animal-specific computational model of pulmonary artery stenosis. *Biomechanics and Modeling in Mechanobiology*. <https://doi.org/10.1007/s10237-024-01850-6>
- Lawrence, N. (2004). Gaussian process latent variable models for visualisation of high dimensional data. In *Advances in neural information processing systems*. 329–336.
- Lawrence, N. (2005). Probabilistic Non-linear Principal Component Analysis with Gaussian Process Latent Variable Models. In *Journal of Machine Learning Research* (Vol. 6).
- Lu, F., Morzfeld, M., Tu, X., & Chorin, A. J. (2015). Limitations of polynomial chaos expansions in the Bayesian solution of inverse problems. *Journal of Computational Physics*, 282, 138–147. <https://doi.org/10.1016/j.jcp.2014.11.010>
- Marzouk, Y. M., & Najm, H. N. (2009). Dimensionality reduction and polynomial chaos acceleration of Bayesian inference in inverse problems. *Journal of Computational Physics*, 228(6), 1862–1902. <https://doi.org/10.1016/j.jcp.2008.11.024>
- Massoud, E. C. (2019). Emulation of environmental models using polynomial chaos expansion. *Environmental Modelling and Software*, 111, 421–431. <https://doi.org/10.1016/j.envsoft.2018.10.008>
- Miles, P. (2019). pymcmcstat: A Python Package for Bayesian Inference Using Delayed Rejection Adaptive Metropolis. *Journal of Open Source Software*, 4(38), 1417. <https://doi.org/10.21105/joss.01417>
- Mora, C., Yousefpour, A., Hosseinmardi, S., & Bostanabad, R. (2024). A gaussian process framework for solving forward and inverse problems involving nonlinear partial differential equations. *Computational Mechanics*. <https://doi.org/10.1007/s00466-024-02559-0>

- Morita, S., Thall, P. F., & Müller, P. (2010). Evaluating the impact of prior assumptions in Bayesian biostatistics. *Statistics in Biosciences*, 2(1), 1–17. <https://doi.org/10.1007/s12561-010-9018-x>
- Mulchrone, A., Kelliham, H. B., Forouzan, O., Hacker, T. A., Bates, M. L., Francois, C. J., & Chesler, N. C. (2019). A Large Animal Model of Right Ventricular Failure due to Chronic Thromboembolic Pulmonary Hypertension: A Focus on Function. *Frontiers in Cardiovascular Medicine*, 5. <https://doi.org/10.3389/fcvm.2018.00189>
- Murray, C. D. (1926). The Physiological Principle of Minimum Work. *Proceedings of the National Academy of Sciences*, 12(3), 207–214. <https://doi.org/10.1073/pnas.12.3.207>
- Myren, S., & Lawrence, E. (2021). A comparison of Gaussian processes and neural networks for computer model emulation and calibration. *Statistical Analysis and Data Mining*, 14(6), 606–623. <https://doi.org/10.1002/sam.11507>
- Nakamura, Y., & Awa, S. (2014). Radius exponent in elastic and rigid arterial models optimized by the least energy principle. *Physiological Reports*, 2(2), e00236. <https://doi.org/10.1002/phy2.236>
- Olufsen, M. S. (1999). *Structured tree outflow condition for blood flow in larger systemic arteries*.
- Olufsen, M. S., Hill, N. A., Vaughan, G. D. A., Sainsbury, C., & Johnson, M. (2012). Rarefaction and blood pressure in systemic and pulmonary arteries. *Journal of Fluid Mechanics*, 705, 280–305. <https://doi.org/10.1017/jfm.2012.220>
- Olufsen, M. S., Peskin, C. S., Kim, W. Y., Pedersen, E. M., Nadim, A., & Larsen, J. (2000). *Numerical Simulation and Experimental Validation of Blood Flow in Arteries with Structured-Tree Outflow Conditions*.
- Paun, L. M., Borowska, A., Colebank, M. J., Olufsen, M. S., & Husmeier, D. (2021). Inference in Cardiovascular Modelling Subject to Medical Interventions. *Proceedings of the International Conference on Statistics*. <https://doi.org/10.11159/icsta21.109>
- Paun, L. M., Colebank, M. J., Olufsen, M. S., Hill, N. A., & Husmeier, D. (2020). Assessing model mismatch and model selection in a Bayesian uncertainty quantification analysis of a fluid-dynamics model of pulmonary blood circulation. *Journal of the Royal Society Interface*, 17(173). <https://doi.org/10.1098/rsif.2020.0886>
- Paun, L. M., Colebank, M. J., Taylor-LaPole, A., Olufsen, M. S., Ryan, W., Murray, I., Salter, J. M., Applebaum, V., Dunne, M., Hollins, J., Kimpton, L., Volodina, V., Xiong, X., & Husmeier, D. (2024). SECRET: Statistical Emulation for Computational Reverse Engineering and Translation with applications in healthcare. *Computer Methods in Applied Mechanics and Engineering*, 430. <https://doi.org/10.1016/j.cma.2024.117193>
- Paun, L. M., & Husmeier, D. (2021). Markov chain Monte Carlo with Gaussian processes for fast parameter estimation and uncertainty quantification in a 1D fluid-dynamics model of the pulmonary circulation. *International Journal for Numerical Methods in Biomedical Engineering*, 37(2). <https://doi.org/10.1002/cnm.3421>
- Paun, L. Mihaela, Mitchel J. Colebank, and Dirk Husmeier. "A comparison of Gaussian processes and polynomial chaos emulators in the context of haemodynamic pulse-wave propagation modelling." To appear, *Philosophical Transactions of the Royal Society A: Mathematical, Physical and Engineering Sciences* (2025).

- Paun, L. M., Qureshi, M. U., Colebank, M., Hill, N. A., Olufsen, M. S., Haider, M. A., & Husmeier, D. (2018). MCMC methods for inference in a mathematical model of pulmonary circulation. *Statistica Neerlandica*, 72(3), 306–338. <https://doi.org/10.1111/stan.12132>
- Pratola, M. T., & Higdon, D. M. (2016). Bayesian Additive Regression Tree Calibration of Complex High-Dimensional Computer Models. *Technometrics*, 58(2), 166–179. <https://doi.org/10.1080/00401706.2015.1049749>
- Qureshi, M. U., Colebank, M. J., Paun, L. M., Ellwein Fix, L., Chesler, N., Haider, M. A., Hill, N. A., Husmeier, D., & Olufsen, M. S. (2019). Hemodynamic assessment of pulmonary hypertension in mice: a model-based analysis of the disease mechanism. *Biomechanics and Modeling in Mechanobiology*, 18(1), 219–243. <https://doi.org/10.1007/s10237-018-1078-8>
- Qureshi, M. U., Vaughan, G. D. A., Sainsbury, C., Johnson, M., Peskin, C. S., Olufsen, M. S., & Hill, N. A. (2014). Numerical simulation of blood flow and pressure drop in the pulmonary arterial and venous circulation. *Biomechanics and Modeling in Mechanobiology*, 13(5), 1137–1154. <https://doi.org/10.1007/s10237-014-0563-y>
- Rasmussen, C. Edward., & Williams, C. K. I. . (2006). *Gaussian processes for machine learning*. MIT Press.
- Shumal, M., Saghafian, M., Shirani, E., & Nili-Ahmadabadi, M. (2024). Novel description for optimality principle of cerebral arteries within the circle of Willis: a Womersley number-based scaling law. *Zeitschrift Fur Angewandte Mathematik Und Physik*, 75(3). <https://doi.org/10.1007/s00033-024-02257-0>
- Singh, D., & Singh, B. (2020). Investigating the impact of data normalization on classification performance. *Applied Soft Computing*, 97. <https://doi.org/10.1016/j.asoc.2019.105524>
- Smith, R. C. (2024). *Uncertainty Quantification: Theory, Implementation, and Applications, Second Edition*. Society for Industrial and Applied Mathematics. <https://doi.org/10.1137/1.9781611977844>
- Spazzapan, M., Sastry, P., Dunning, J., Nordsletten, D., & de Vecchi, A. (2018). The use of biophysical flow models in the surgical management of patients affected by Chronic Thromboembolic Pulmonary Hypertension. *Frontiers in Physiology*, 9(MAR). <https://doi.org/10.3389/fphys.2018.00223>
- Taylor-Lapole, A. M., Mihaela Paun, L., Lior, D., Weigand, J. D., Puelz, C., & Olufsen, M. S. (2024). *Parameter selection and optimization of a computational network model of blood flow in single-ventricle patients*.
- Teckentrup, A. L. (2020). Convergence of gaussian process regression with estimated hyper-parameters and applications in bayesian inverse problems. *SIAM-ASA Journal on Uncertainty Quantification*, 8(4), 1310–1337. <https://doi.org/10.1137/19M1284816>
- Tsubata, H., Nakanishi, N., Itatani, K., Takigami, M., Matsubara, Y., Ogo, T., Fukuda, T., Matsuda, H., & Matoba, S. (2023). Pulmonary artery blood flow dynamics in chronic thromboembolic pulmonary hypertension. *Scientific Reports*, 13(1), 6490. <https://doi.org/10.1038/s41598-023-33727-6>
- Uylings, H B M. (1977). Optimization of Diameters and Bifurcation Angles in Lung and Vascular Tree Structures." *Bulletin of Mathematical Biology (Vol. 39)*

- Wei, F. F., Wu, Y., Xue, R., Liu, X., He, X., Dong, B., Zhen, Z., Chen, X., Liang, W., Zhao, J., He, J., Dong, Y., Staessen, J. A., & Liu, C. (2022). Clinical significance of mean and pulse pressure in patients with heart failure with preserved ejection fraction. *Hypertension*, *79*(1), 241–250. <https://doi.org/10.1161/HYPERTENSIONAHA.121.17782>
- Wentworth, M. T., Smith, R. C., & Williams, B. (2018). Bayesian model calibration and uncertainty quantification for an HIV model using adaptive Metropolis algorithms. *Inverse Problems in Science and Engineering*, *26*(2), 233–256. <https://doi.org/10.1080/17415977.2017.1312365>
- Yang, W., Hanley, F. L., Chan, F. P., Marsden, A. L., Vignon-Clementel, I. E., & Feinstein, J. A. (2018). Computational simulation of postoperative pulmonary flow distribution in Alagille patients with peripheral pulmonary artery stenosis. *Congenital Heart Disease*, *13*(2), 241–250. <https://doi.org/10.1111/chd.12556>
- Yin, M., Yazdani, A., & Karniadakis, G. E. (2019). One-dimensional modeling of fractional flow reserve in coronary artery disease: Uncertainty quantification and Bayesian optimization. *Computer Methods in Applied Mechanics and Engineering*, *353*, 66–85. <https://doi.org/10.1016/j.cma.2019.05.005>
- Zambrano, B. A., McLean, N. A., Zhao, X., Tan, J. Le, Zhong, L., Figueroa, C. A., Lee, L. C., & Baek, S. (2018). Image-based computational assessment of vascular wall mechanics and hemodynamics in pulmonary arterial hypertension patients. *Journal of Biomechanics*, *68*, 84–92. <https://doi.org/10.1016/j.jbiomech.2017.12.022>
- Zanjani Foumani, Z., Shishehbor, M., Yousefpour, A., & Bostanabad, R. (2023). Multi-fidelity cost-aware Bayesian optimization. *Computer Methods in Applied Mechanics and Engineering*, *407*. <https://doi.org/10.1016/j.cma.2023.115937>

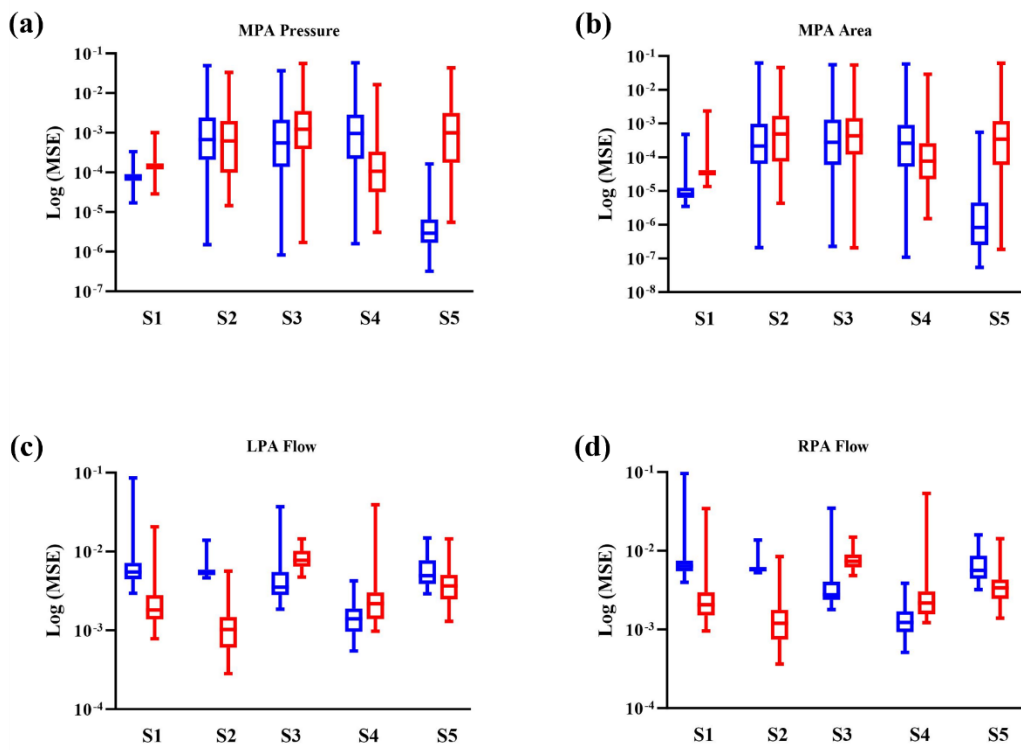


Figure 3 GP emulator Vs. PDE simulator.

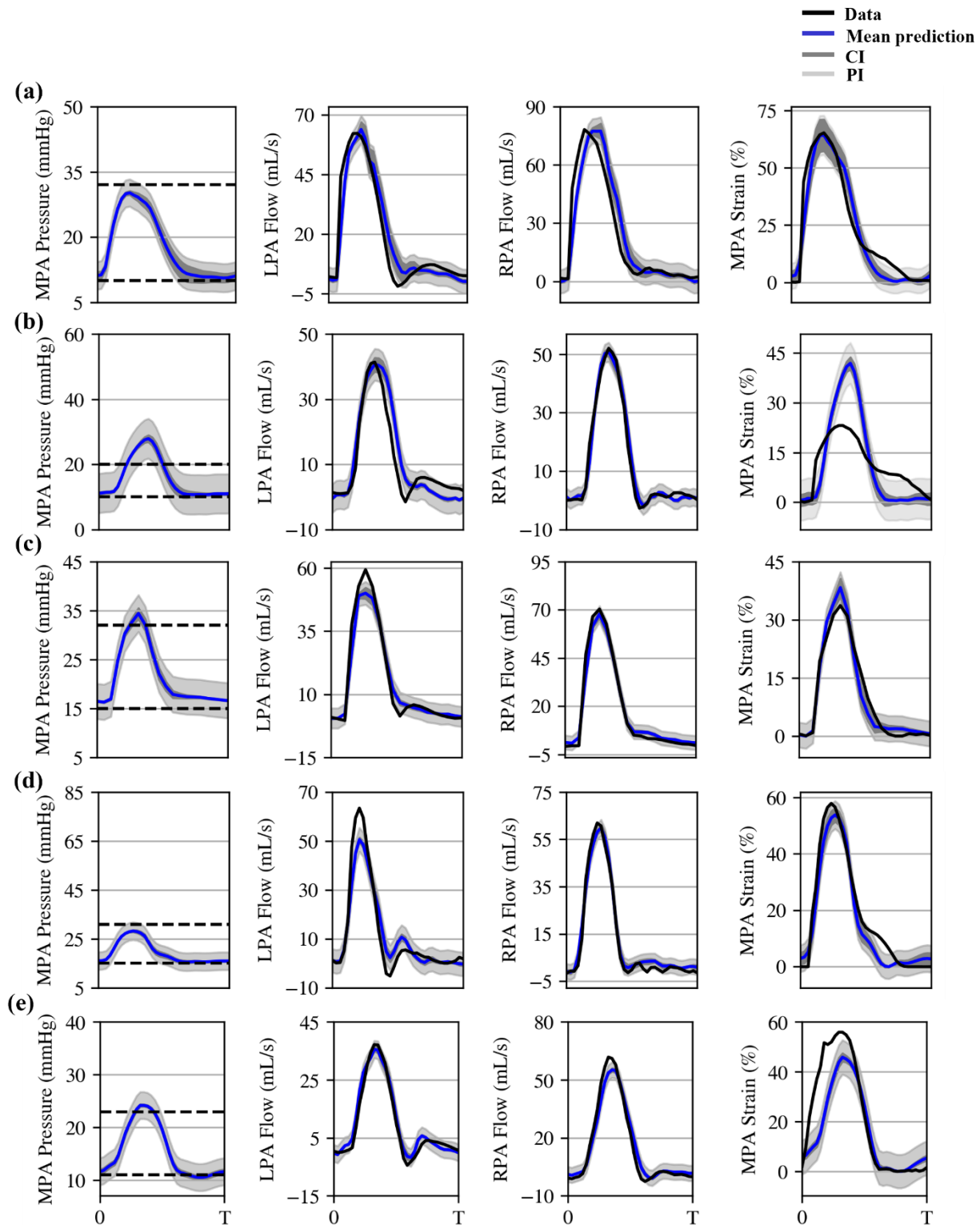


Figure 4 Calibration results for all subjects in Baseline. The figure shows measured data across all four sources (black), GP predictions at the posterior mean (blue), the credible interval (CI) (dark gray), and the prediction interval (PI) (light gray). Subplots are organized as follows: (a) S1, (b) S2, (c) S3, (d) S4, and (e) S5.

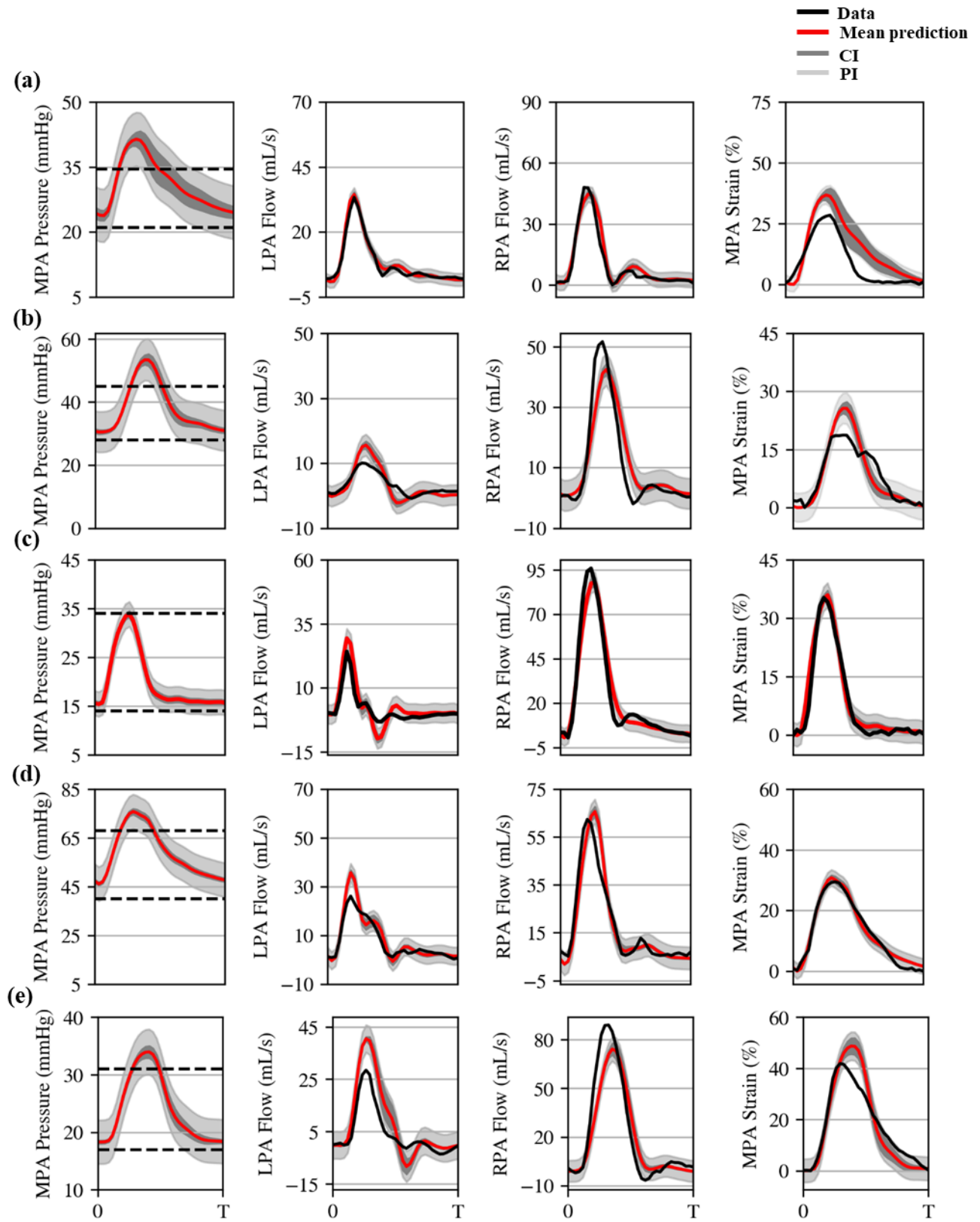


Figure 5 Calibration results for all subjects in CTEPH. The figure shows measured data across all four sources (black), GP predictions at the posterior mean (red), the credible interval (CI) (dark gray), and the prediction interval (PI) (light gray). Subplots are organized as follows: (a) S1, (b) S2, (c) S3, (d) S4, and (e) S5.

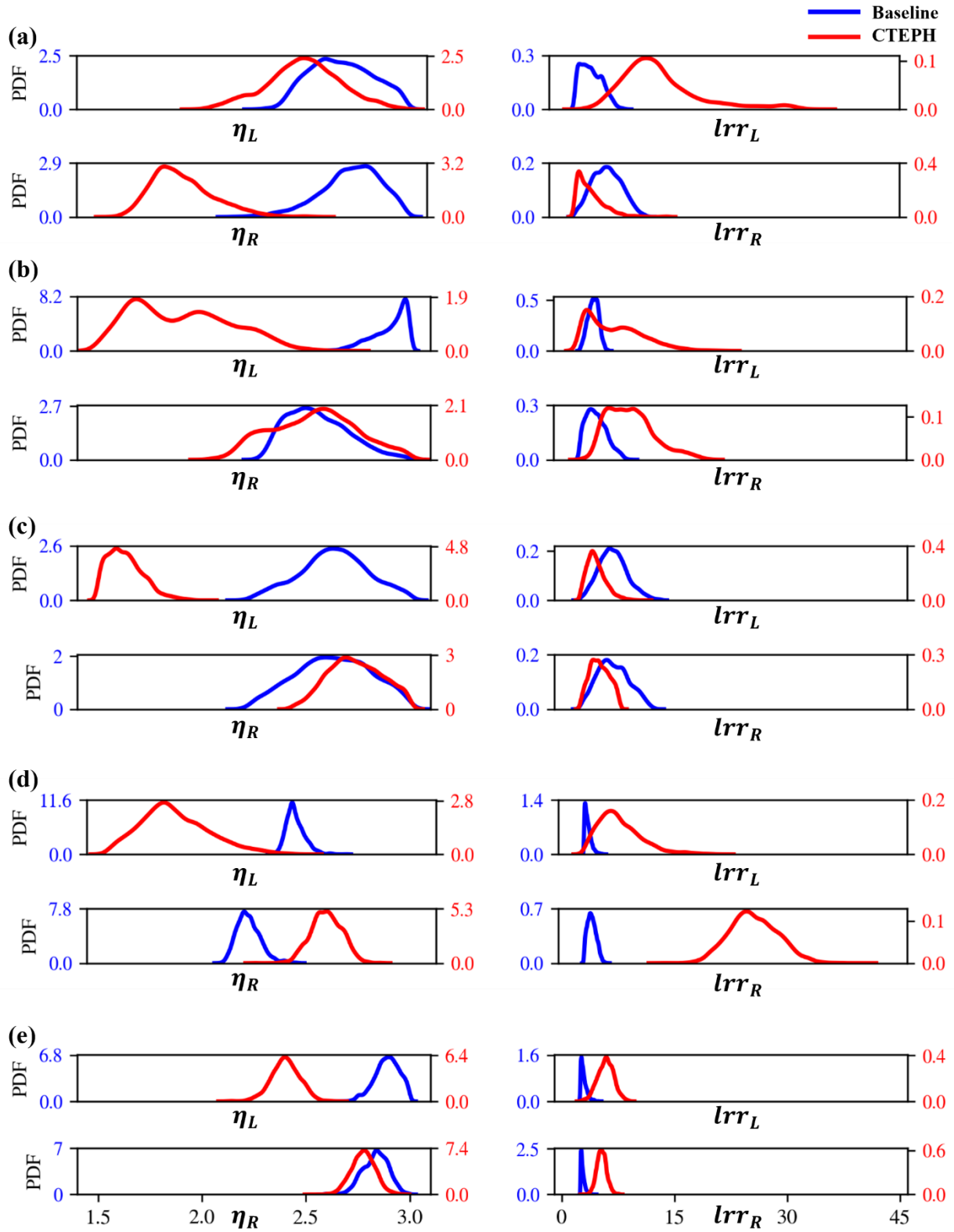


Figure 6 Marginal posterior distributions of the ST parameters for all subjects, shown for baseline (blue) and CTEPH (red). Subplots are organized as follows: (a) S1, (b) S2, (c) S3, (d) S4, and (e) S5.

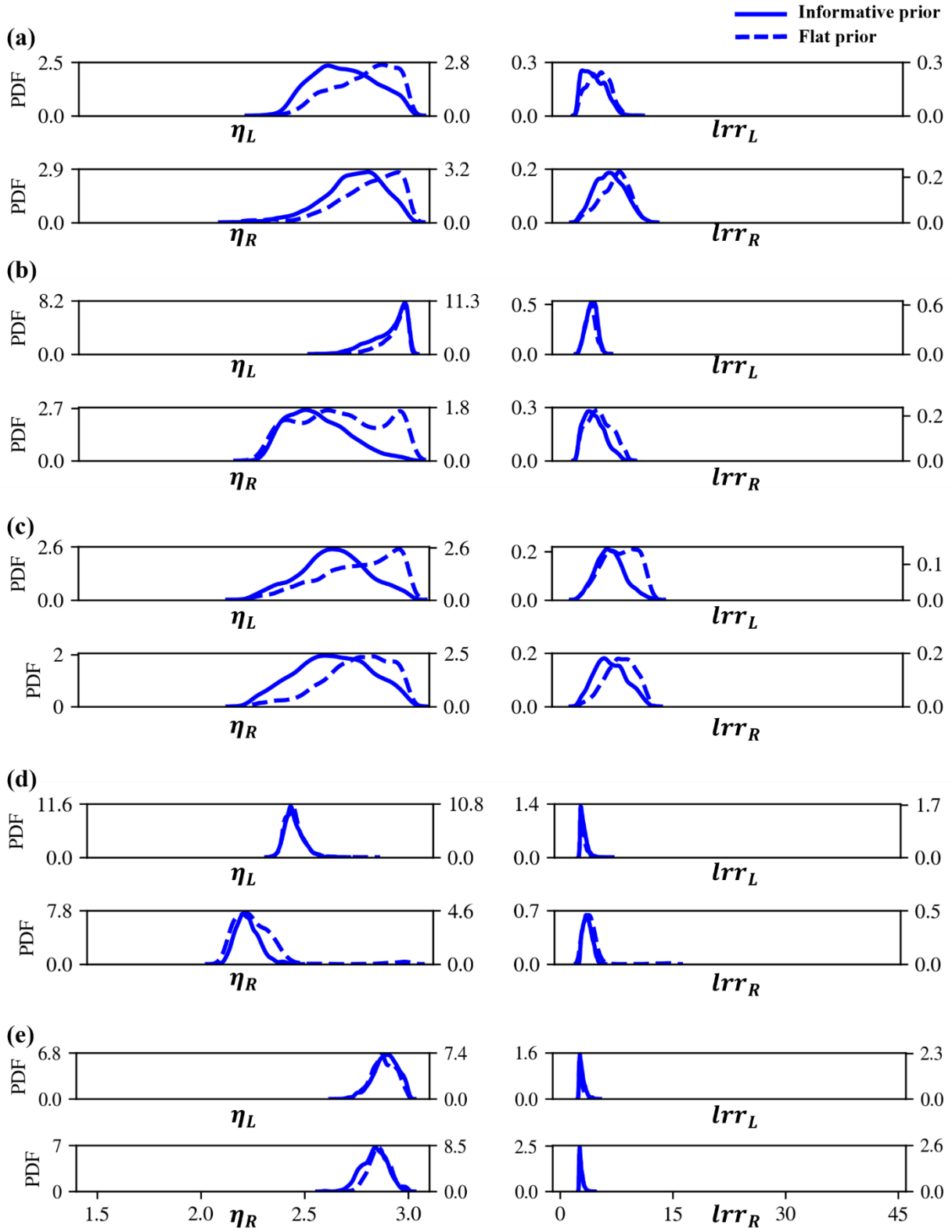


Figure 7 Informative prior impact on the marginal posteriors in baseline. The left y-axis represents informative prior PDF, and the right y-axis represents flat prior PDF. Subplots are organized as follows: (a) S1, (b) S2, (c) S3, (d) S4, and (e) S5.

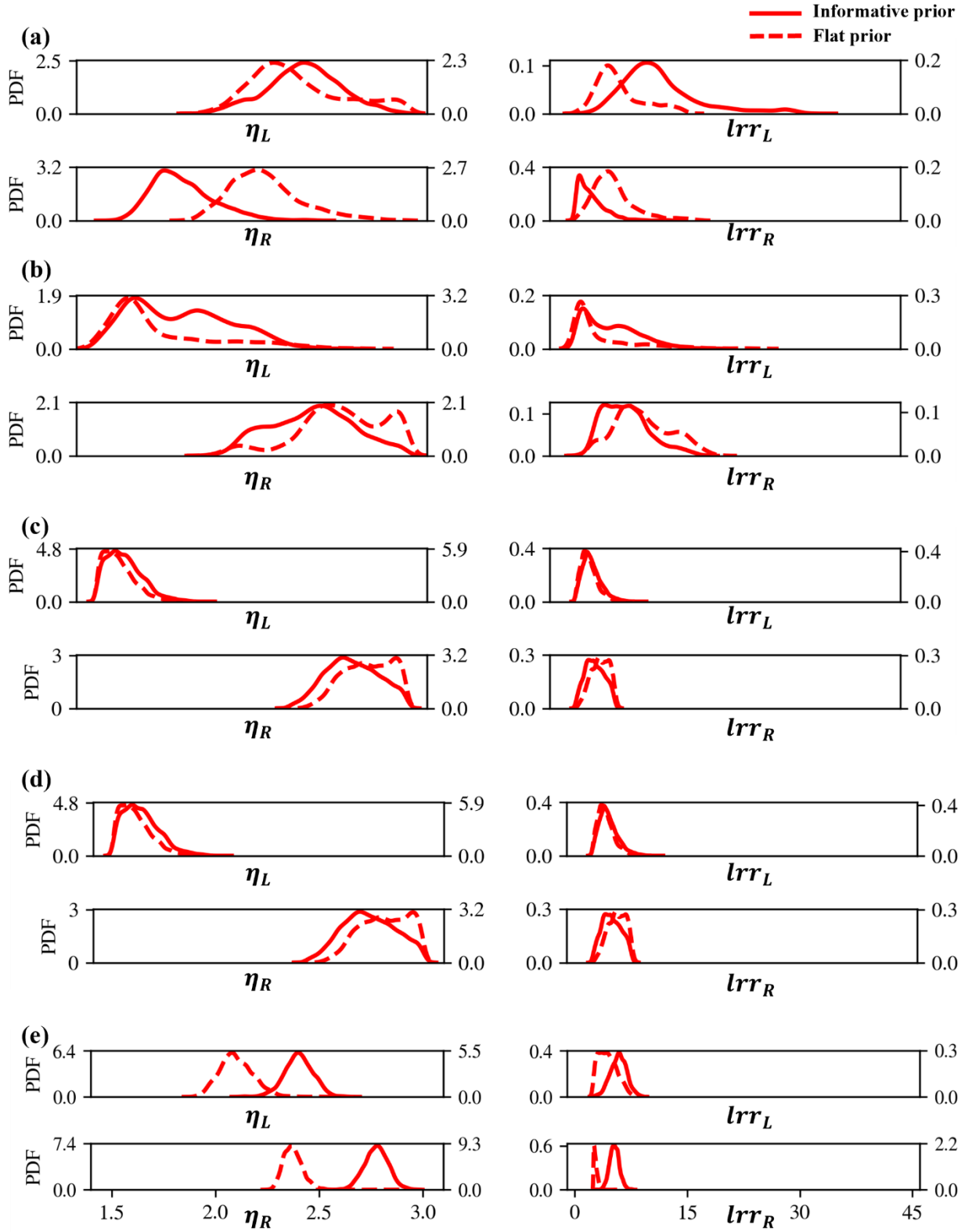


Figure 8 Informative prior impact on the marginal posteriors in CTEPH. The left y-axis represents informative prior PDF, and the right y-axis represents flat prior PDF. Subplots are organized as follows: (a) S1, (b) S2, (c) S3, (d) S4, and (e) S5.

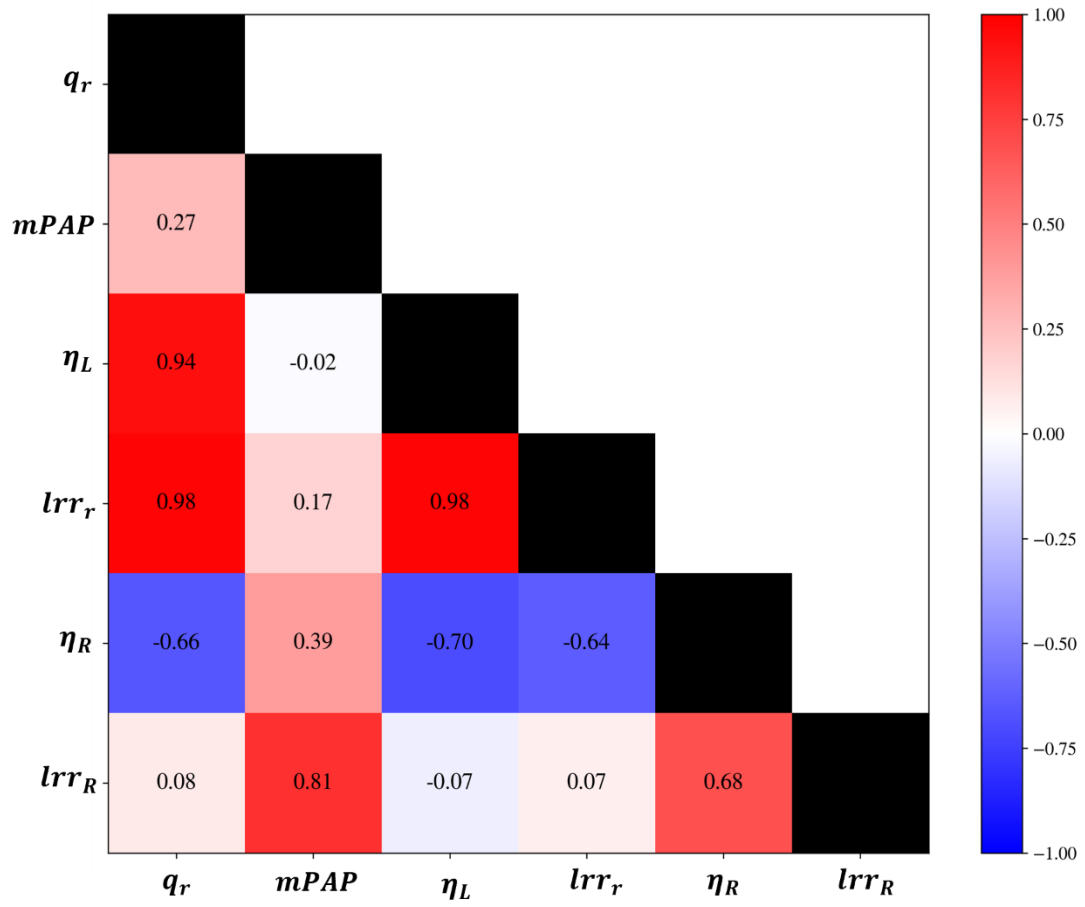


Figure 9 Correlation analysis for the model outputs.